Excitation of SST anomalies in the eastern equatorial Pacific by oceanic optimal perturbations

by Florian Sévellec[1,2] and Alexey V. Fedorov[1]

ABSTRACT

A generalized stability analysis is used to explore the excitation of sea-surface temperature anomalies in the eastern equatorial Pacific by optimal initial perturbations in temperature and salinity within an ocean general circulation model. We find perturbations that can efficiently modify the SST of the Nino3 region with an approximately 9-month delay. The time interval between the end of March and mid-April is particularly favorable for these perturbations to cause subsequent changes in the eastern equatorial Pacific. This sensitivity is related to two critical factors: during the boreal spring Equinox the heat content of the western equatorial Pacific reaches its seasonal maximum, whereas the zonal winds along the equator relax.

The optimal initial anomalies in temperature and salinity have a complex spatial structure extending between 20°S and 20°N. This large meridional extent of the anomalies allows for a strong focusing effect - signals from different locations reach the eastern equatorial Pacific simultaneously thus generating a strong transient warming in a relatively small region. Ocean adjustment to the optimal perturbations involves a basin-size Rossby wave that propagates westward and induces a large-scale anomalous eastward advection along the equator, which acts on the mean east-west temperature gradient and gradually warms SST in the east. At the same time, a continuum of Kelvin waves are being excited, which reduce the thermocline slope along the equator and deepen the thermocline in the eastern equatorial Pacific. Thus, the Rossby wave and Kelvin waves work constructively to generate the transient warming of the Nino3 SST. An idealized model with two variables is formulated to illustrate these ideas and, in particular, show the importance of zonal advection feedback for the amplitude and duration of the transient warming. Ultimately, this study highlights the importance of non-normal dynamics for generating an efficient transient growth of SST anomalies in the tropical Pacific even in the absence of coupled ocean-atmosphere interactions.

1. Introduction

Variations in Sea-Surface Temperature (SST) of the eastern equatorial Pacific, reflected for example in the Nino3 index, are a key element of the El Niño - Southern Oscillation (ENSO) - the dominant climate mode in the tropical Pacific (e.g., Fedorov and Philander, 2000; Clarke, 2008; Guilyardi *et al.*, 2009). While coupled ocean-atmosphere interactions are of critical importance for this climate mode, a number of aspects of ENSO are related

1. Department of Geology and Geophysics, Yale University, New Haven, Connecticut 06520, U.S.A.
2. Corresponding author. *email: florian.sevellec@yale.edu*

to ocean dynamics (e.g., Fedorov, 2010). The goal of the present study is to explore the role of ocean dynamics in the transient growth of equatorial SST anomalies that can be excited in the tropical Pacific by optimal initial perturbations in temperature and salinity fields. Such initial perturbations will lead to a strong transient increase of the SST in the eastern equatorial Pacific after a prescribed time delay (several months to years) even in the absence of coupled ocean-atmosphere interactions.

To calculate optimal perturbations we will use a realistic ocean general circulation model (OPA) and apply the generalized stability analysis as the major tool of the study. The generalized stability analysis for autonomous operators (the background state is independent of time) was discussed by Farrell and Ioannou (1996a) and for nonautonomous systems (the background state evolves with time) by Farrell and Ioannou (1996b). Because of advective as well as diffusive processes, the ocean dynamics is typically non-normal (e.g., Farrell and Moore, 1992). This implies that the fastest growing (or least-damped) eigenmode, obtained by the classical linear stability analysis, does not necessarily produce the fastest growth over a finite time interval. In fact, perturbations leading to the fastest growth can have a spatial structure very different from the eigenmodes. Therefore, to understand the transient growth of a perturbation, rather than its asymptotic behavior, one must use the generalized stability analysis that takes into account the non-normality of the system and allows an expedite calculation of optimal initial perturbations in a linear framework.

Previously, the generalized stability analysis was used in an oceanic context by Farrell and Moore (1992) and Moore and Farrell (1993) to find the most rapidly growing perturbation of a quasi-geostrophic ocean model representing the Gulf Stream. In the context of ENSO, the excitation of El Niño-like variability by optimal perturbations in an intermediate coupled model was discussed by Moore and Kleeman (1999, 2001) and in a hierarchy of hybrid coupled models by (Moore *et al.*, 2003), just to name a few studies. In a forced oceanic context, but focusing on the Atlantic (using an idealized basin configuration), Zanna *et al.* (2010) show the existence of transient growth of tropical SST. Recently, Sévellec *et al.* (2007, 2008) developed an efficient method for calculating the structure of the optimal perturbations in ocean GCMs (originally in application to the Atlantic meridional overturning circulation). Building on their results, here we will apply a similar analysis to study the excitation of SST anomalies in the eastern equatorial Pacific by initial optimal perturbations in the ocean temperature and salinity fields.

As we will demonstrate, this transient growth, and the problem of optimal perturbations in general, are relevant to the seasonal phase-locking and the spring predictability barrier associated with the development of SST anomalies in the eastern equatorial Pacific, even in the absence of coupled ocean-atmosphere feedbacks.

It has been long recognized that El Niño events peak during boreal winter (e.g., Rasmusson and Carpenter, 1982; Wallace *et al.*, 1998), even though particular months of the maximum temperature can vary significantly from one event to the next (Neelin *et al.*, 2000). The spring predictability barrier for ENSO is typically defined as the sharp drop in the SST lagged autocorrelation (persistence) around April regardless of the starting month (the

month of zero lag), e.g., Torrence and Webster (1998). In practical terms, this means that before April it is difficult for climate models to predict whether an El Niño is going to take place during the rest of the year.

Tziperman *et al.* (1997) discuss three major causes for the seasonal phase-locking: the annual cycle of the climatological wind divergence, SSTs, and ocean upwelling, but emphasize the seasonal cycle in SST as crucial for the precise locking if ENSO to the end of the calendar year. Tziperman *et al.* (1998) also discuss the seasonally-varying strength of the ocean-atmosphere coupling (Bjerknes, 1969) as an alternative cause. Despite these and other studies, the ultimate causes for both the phase-locking and the seasonal predictability barrier are still debated.

It is likely, however, that the phase-locking and the seasonal predictability barrier are related: in observations, decades with stronger seasonal phase-locking typically have a stronger predictability barrier as well (Balmaseda *et al.*, 1995; Flügel and Chang, 1999). Blumenthal (1991) and Xue *et al.* (1994) argued that the error growth in the system (a reason for the predictability barrier) and the ENSO locking to the seasonal cycle are affected by the same dynamics. These studies also suggest that the two phenomena can be studied in a linear context. More recently, Thompson and Battisti (2000) and Thompson and Battisti (2001) have demonstrated that both the phase-locking and the seasonal predictability barrier exist in a linearized version of an intermediate coupled model (a version of the model of Zebiak and Cane, 1987), as long as the linearization is made with respect to the seasonally-varying mean state of the system. Taking nonlinearity into account would improve the agreement between the model and the observations but was not essential.

Here, we will ask the next question: To what extent these two effects can be reproduced by oceanic mechanisms alone? In particular, could the error growth for SST anomalies be controlled by ocean dynamics? To answer these questions we will use an ocean general circulation model (and its tangent linear and adjoint versions) and calculate oceanic optimal perturbations in temperature and salinity fields for equatorial SST anomalies. These perturbations will provide the most efficient way to change temperatures in the Nino3 region, thus setting the upper bound on the SST error growth solely due to ocean dynamics.

We should also emphasize that nowhere in our paper do we claim that ocean-atmosphere interactions are not important for ENSO and tropical climate variability in general. Rather, the limited goal of the study is to demonstrate that even in the ocean-only context there exist perturbations in the system that can efficiently excite El Niño-like SST anomalies - amplified by ocean-atmosphere feedbacks those anomalies can potentially develop into full El Niño events.

The structure of the paper is as follows. First, we describe the ocean model and the seasonally-varying basic state it produces (Section 2). In Section 3, we perform a generalized stability analysis for the ocean model and describe the optimal initial perturbations and ocean response to the perturbations. Next, we introduce a simple idealized model designed to better understand the key mechanisms of the optimal growth (Section 4). Finally, in Section 5 we discuss our findings and propose further outlook.

2. The ocean model and ocean background state

a. The model and configuration

The ocean GCM in this study is OPA 8.2 (Océan PArallélisé, Madec *et al.*, 1998) in its 2°
global configuration (ORCA2, Madec and Imbard, 1996). It uses the rigid-lid approximation
and the z-coordinates with 31 levels in the vertical - the layer thickness varies from 10 m at
the surface to 500 m at depth. The model is integrated using the Arakawa C-grid.

The present model configuration employs the following parameterizations: convection is
parameterized by an increase in the vertical diffusion when the ocean vertical stratification
is unstable; double diffusion is taken into account by two different terms for mixing tem-
perature and salinity; eddy-induced velocities are described by the Gent and McWilliams
(1990) approximation; the viscosity coefficient follows the turbulent closure scheme of
Blanke and Delecluse (1993) and are functions of longitude, latitude and depth; and the
mixing coefficient for temperature and salinity vary in longitude and latitude (Redi, 1982).

The linear and adjoint models are provided by the OPATAM code (OPA Tangent Adjoint
Model, Weaver *et al.*, 2003). The tangent linear model is a linearization of the OPA's
primitive equations of motions with respect to the ocean seasonally-varying basic state.

For the present study, we impose surface heat and freshwater fluxes and do not use surface
restoring. These fluxes were computed by running the full nonlinear model forced with a
combination of the prescribed climatological fluxes and restoring terms (restoring to the
climatological seasonal cycle). This approach produces a realistic seasonal cycle for the
linear and adjoint models, but reduces the damping and allows SST anomalies to develop
more easily (Huck and Vallis, 2001; Arzel *et al.*, 2006; Sévellec *et al.*, 2009), for details see
below.

Several additional approximations have been introduced for the tangent-linear and adjoint
models: the viscosity coefficients, the tracer mixing coefficients, and the eddy-induced
advection, are calculated only for the basic ocean state - further variations in those coeffi-
cients are not allowed.

b. The ocean background state

The seasonally-varying basic state of the ocean, here also referred to as the annual model
"trajectory," is obtained by the direct integration of the OPA model subject to climatological
surface boundary forcing (varying with the annual cycle). In particular, we used the ECMWF
heat fluxes averaged in the interval from 1979 to 1993, the ERS wind stress blended with
the TAO data between 1993–1996, and an estimate of the climatological river runoff. In
addition, we applied a surface temperature restoring to the Reynolds climatological values
averaged from 1982 to 1989, together with a surface salinity restoring to the Levitus (1989)
climatology (we emphasize that no restoring was used in the tangent linear and adjoint
models). A mass restoring term to the Levitus climatological values of temperature and
salinity was applied in the Red and Mediterranean seas. Starting with the Levitus climatology
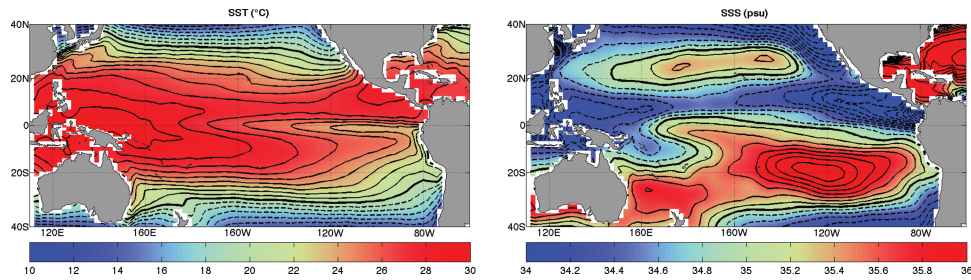
Figure 1. The annual mean basic state of the ocean as simulated by the GCM: (left) sea surface temperature and (right) sea surface salinity (averaged over the upper 10 m of the ocean). Contour intervals are 1°C and 0.2 psu. Thick lines correspond to 20°C or 35 psu, respectively.
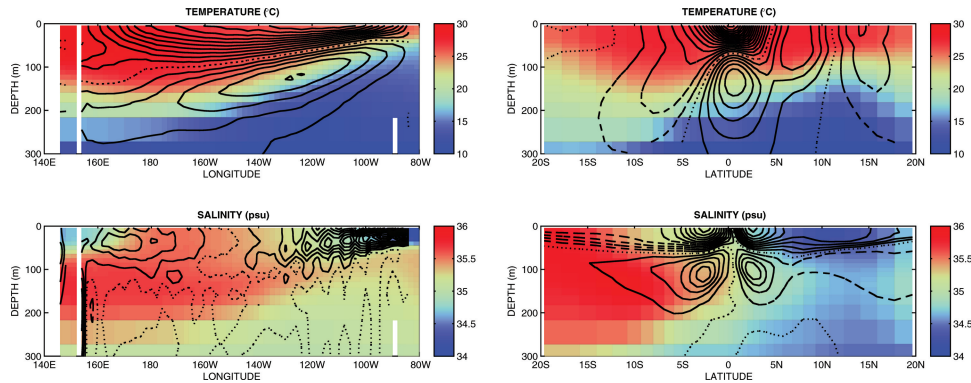

Figure 2. The annual mean basic state of the ocean as simulated by the GCM. (Top) ocean temperature and zonal velocity as a function of (left) longitude and depth and (right) latitude and depth. (Bottom) ocean salinity and meridional velocity as a function of (left) longitude and depth and (right) latitude and depth. Variables in the left panels are averaged between 5°S and 5°N, whereas variables in the right panels are averaged from west to east over the Pacific basin. Colors indicate temperature or salinity; contour lines indicate velocity. Solid, dashed and dotted lines represent positive, negative and zero values, respectively. Contour intervals are 3×10^{-2} m s^{-1} for the zonal velocity and 6×10^{-3} m s^{-1} for the meridional velocity.

as the initial conditions, the model produces a quasi-stationary annual cycle in the ocean basic state after 200 years of integration.

The obtained basic state of the ocean (Fig. 1) is characterized by a pronounced cold tongue in the eastern and central equatorial Pacific and a warm pool in the west. Coastal upwelling along the coast of South America is well represented. Interhemispheric differences in sea-surface salinity associated with the Inter-Tropical Convergence Zone (ITCZ) are also evident.

Equatorial sections (Fig. 2) show the Western Pacific warm pool, the equatorial thermocline sloping from west to east, and the Equatorial UnderCurrent (EUC) whose signature

is clear in the distribution of salinity at around 100-m depth in the longitude-depth section. Even though the ocean flow is dominated by zonal currents, meridional velocities reveal the presence of local tropical cells that upwell water to the surface near the equator.

In response to seasonal changes in heat and freshwater fluxes and wind stress, the model exhibits a robust annual cycle (Fig. 3). The cold tongue strengthens around October but weakens in March. The ITCZ is farther away from the equator in October but gets closer to the equator in March.

Now that we have obtained a realistic seasonally-varying basic state of the ocean we will conduct a generalized stability analysis of this basic state. In particular, we will explore how perturbations in ocean temperature and salinity imposed during different times (and different seasons) generate a warming of sea surface in the eastern equatorial Pacific.

3. Optimal initial perturbations of the Nino3 index

a. Generalized stability analysis

The prognostic equations employed by any GCM can be written as a general non-autonomous dynamical system:

$$d_t|U\rangle = \mathcal{N}(|U\rangle, t), \tag{1}$$

where $\mathcal{N}$ is a time-dependent nonlinear operator and $|U\rangle$ the state vector consisting of all prognostic variables (including ocean temperature, salinity, and velocity). We can also define the $\langle U|$ through the Euclidean scalar product $\langle U|U\rangle$.

We decompose the state vector as $|U\rangle = |\bar{U}\rangle + |u\rangle$, where $|\bar{U}\rangle$ is the seasonally-varying basic state (the nonlinear trajectory) and $|u\rangle$ is a perturbation with respect to this basic state. The time evolution of the perturbation is described by a nonautonomous system of equations:

$$d_t|u\rangle = \mathbf{A}(t)|u\rangle, \ \ \mathbf{A}(t) = \left.\frac{\partial \mathcal{N}}{\partial |U\rangle}\right|_{|\bar{U}\rangle}, \tag{2}$$

where $\mathbf{A}(t)$ is the Jacobian matrix, which is a function of the annual trajectory $|\bar{U}\rangle$. We can integrate this last relation to obtain the time evolution of the perturbation as (Farrell and Ioannou, 1996b):

$$|u(t_2)\rangle = \int_{t_1}^{t_2} dt \, \mathbf{A}(t)|u(t_1)\rangle = \mathbf{M}(t_2, t_1)|u(t_1)\rangle, \tag{3}$$

where $\mathbf{M}(t_2, t_1)$ is called the propagator of the linearized dynamics from the time t_1 to t_2.

The measure that we choose to maximize is the Nino3 index: sea-surface temperature in the eastern equatorial Pacific averaged over the region 5°S–5°N latitude, 150°W–90°W longitude. This index is a common measure of ENSO - its positive values indicate El Niño (or a warming of the eastern equatorial Pacific) and its negative values indicate La Niña
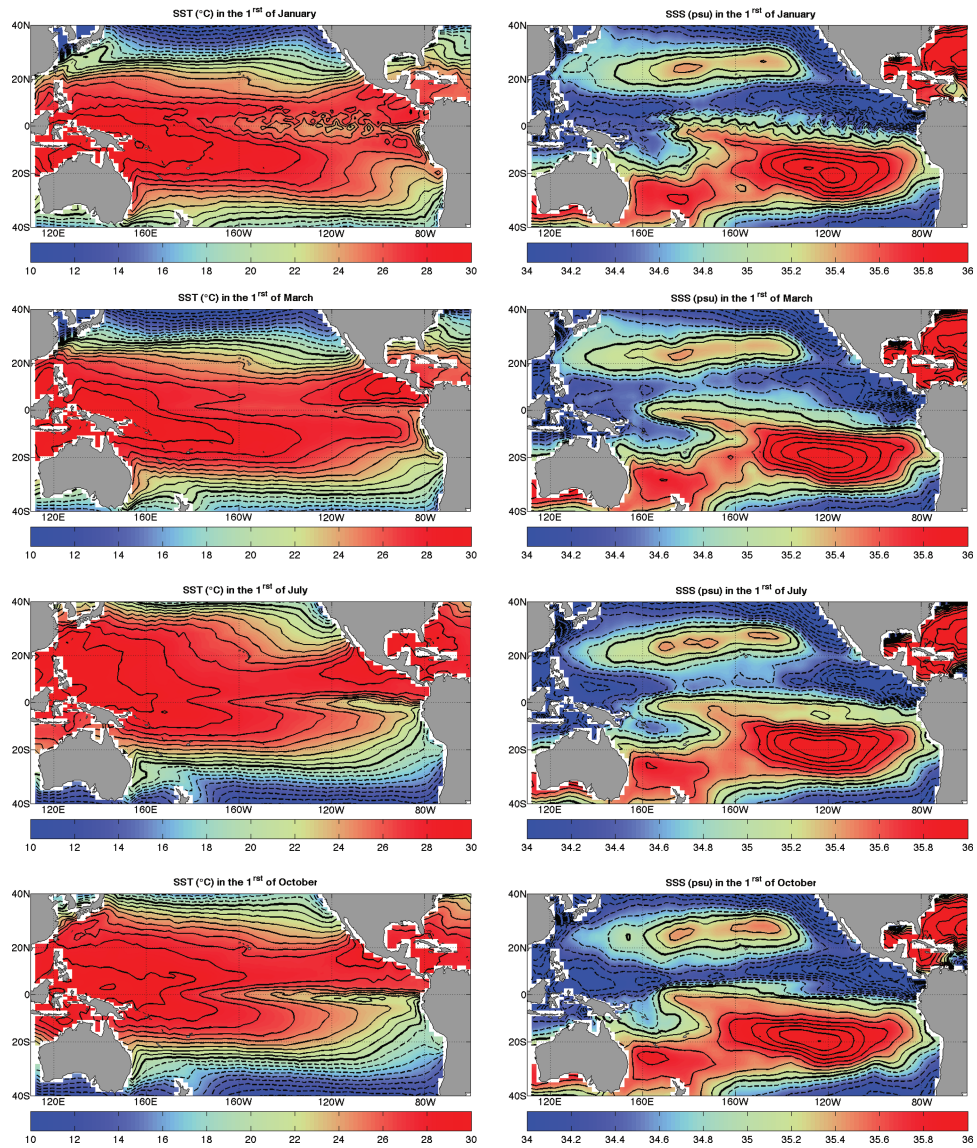
Figure 3. (Left) sea-surface temperature and (right) sea-surface salinity at different phases of the seasonal cycle as simulated by the GCM: (from top to bottom) snapshots for the 1st of January, March, July and October. The thick lines represent 20°C or 35 psu. Solid and dashed lines represent higher and lower values, respectively, with a contour interval of 1 K or 0.2 psu.

(a cooling of the west equatorial Pacific). Using this index, we define the cost function of the optimization procedure as:

$$\langle \boldsymbol{F} | \boldsymbol{u} \rangle = \int_{5°S}^{5°N} \int_{90°W}^{150°W} ds\, T(x, y, 0, t), \tag{4}$$

where T is the temperature perturbation a function of longitude x, latitude y, depth z, and time t (z is set to zero in this expression). To limit our analysis to initial anomalies only in temperature and salinity, we define the operator $\mathbf{P}$ that constraints the full state vector, such as: $|\boldsymbol{u}\rangle = \mathbf{P}|\boldsymbol{u}'\rangle$, where $|\boldsymbol{u}'\rangle$ is the temperature and salinity vector.

Now, we define a norm for this temperature-salinity vector:

$$\langle \boldsymbol{u} | \mathbf{N} | \boldsymbol{u} \rangle = \langle \boldsymbol{u}' | \mathbf{P}^\dagger \mathbf{N} \mathbf{P} | \boldsymbol{u}' \rangle = \langle \boldsymbol{u}' | \mathbf{S} | \boldsymbol{u}' \rangle = \frac{\iiint dv\, [(\alpha T)^2 + (\beta S)^2]}{\iiint dv}, \tag{5}$$

where $\dagger$ denotes an adjoint to an operator (defined with respect to the Euclidean scalar product: $\langle \boldsymbol{u}_1 | \mathbf{L} | \boldsymbol{u}_2 \rangle = \langle \boldsymbol{u}_2 | \mathbf{L}^\dagger | \boldsymbol{u}_1 \rangle$, where $|\boldsymbol{u}_1\rangle$ and $|\boldsymbol{u}_2\rangle$ are two state vectors and $\mathbf{L}$ is a linear operator), dv is the unit volume, T - the temperature anomaly, S - the salinity anomaly, α and β are the thermal expansion and the haline contraction coefficients. This norm describes the departure in term of density of a three-dimensional temperature-salinity anomaly from the annual trajectory of the system. $\mathbf{N}$ and $\mathbf{S}$ are the norm operators defined in the state-vector space and temperature-salinity subspace, respectively.

Note that there is some confusion in literature as for what exactly the terms cost function and norm should be used. In this study, the cost function is a measure of what we would like to maximize (the Nino3 SST index), and the norm is a measure of the perturbation (in terms of density anomaly).

We now define the Lagrangian function as:

$$\mathcal{L}(t_i, t_m) = \langle \boldsymbol{F} | \boldsymbol{u}(t_m) \rangle - \gamma \langle \boldsymbol{u}(t_i) | \mathbf{N} | \boldsymbol{u}(t_i) \rangle, \tag{6}$$

where t_i is the initial time (the time when the optimal initial perturbation is applied), t_m the maximization time (the time when the cost function reaches to its maximum) and γ is a Lagrange multiplier. This Lagrangian function allows us to maximize the cost function subject to the normalization constraint:

$$\langle \boldsymbol{u}(t_i) | \mathbf{N} | \boldsymbol{u}(t_i) \rangle - 1 = 0. \tag{7}$$

Using (6), (7) and the maximization condition $d\mathcal{L}=0$, the optimal initial perturbations can be obtained as:

$$\left| \boldsymbol{u}_{\{t_i, t_m\}}^{\text{opt}}(t_i) \right\rangle = \pm \frac{\mathbf{P}\mathbf{S}^{-1}\mathbf{P}^\dagger \mathbf{M}^\dagger(t_i, t_m)|\boldsymbol{F}\rangle}{\sqrt{\langle \boldsymbol{F} | \mathbf{M}(t_m, t_i)\mathbf{P}\mathbf{S}^{-1}\mathbf{P}^\dagger \mathbf{M}^\dagger(t_i, t_m)|\boldsymbol{F}\rangle}}, \tag{8}$$
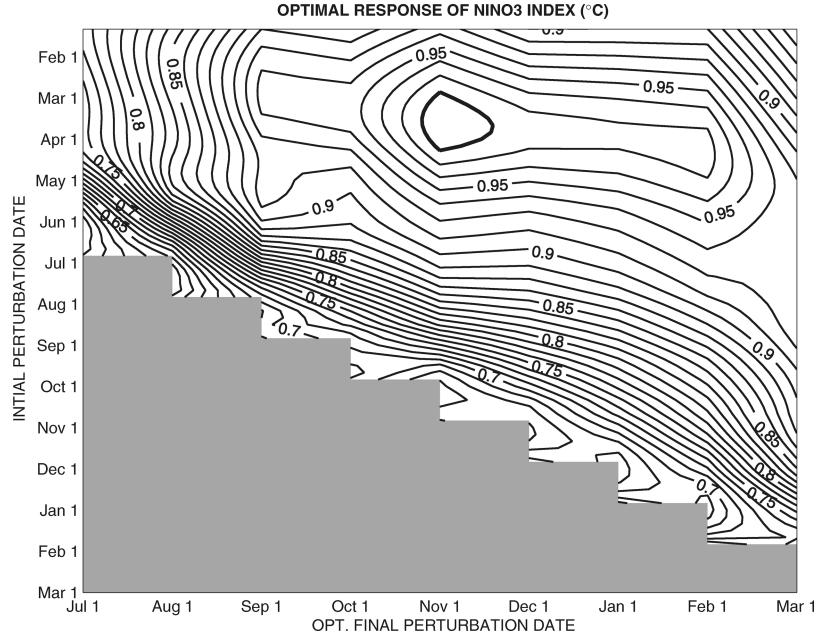
OPTIMAL RESPONSE OF NINO3 INDEX (°C)

Figure 4. The optimal response of the Nino3 SST index, $\langle F | u^{\mathrm{opt}}_{\{t_i,t_m\}}(t_m) \rangle$, as a function of the initialization time (t_i), i.e., the time when a perturbation was applied (the vertical axis), and the optimization time (t_m), i.e., the time when the maximum warming is achieved (the horizontal axis), see equation (8). All initial perturbations are rescaled in exactly the same way so that the greatest change of the Nino3 index is 1°C. Contour intervals are 1.25×10^{-2}°C and the thick line indicates a range of values close to the maximum (temperature increase larger than 0.985°C. In the gray area $t_m < t_i$.

and the system response at time t_m as

$$\langle F | u^{\mathrm{opt}}_{\{t_i,t_m\}}(t_m) \rangle = \langle F | \mathbf{M}(t_m, t_i) | u^{\mathrm{opt}}_{\{t_i,t_m\}}(t_i) \rangle = \pm \sqrt{\langle F | \mathbf{M}(t_m, t_i) \mathbf{P} \mathbf{S}^{-1} \mathbf{P}^{\dagger} \mathbf{M}^{\dagger}(t_i, t_m) | F \rangle}. \quad (9)$$

This solution depends on both the initial time and the maximization time. It means that the optimal solutions initialized in December and September, for example, are *a priori* not the same. To test that, we have performed a set of calculations based on (9) and varying the maximization times and initial dates within one calendar year (Fig. 4).

The first general result of the calculations is that different optimal perturbations can induce a transient growth that will alter the Nino3 SST after an arbitrary-chosen time delay - from a few weeks to several years (Fig. 4 and Fig. 5, top panel). This is related to the variety of processes acting in the tropical ocean on different time scales, including equatorial wave dynamics, advection, dissipative effects, etc.

The second important result is that seasonality affects the growth - the optimal response of the Nino3 index is strongest for initialization times, t_i, from end of March to mid-April

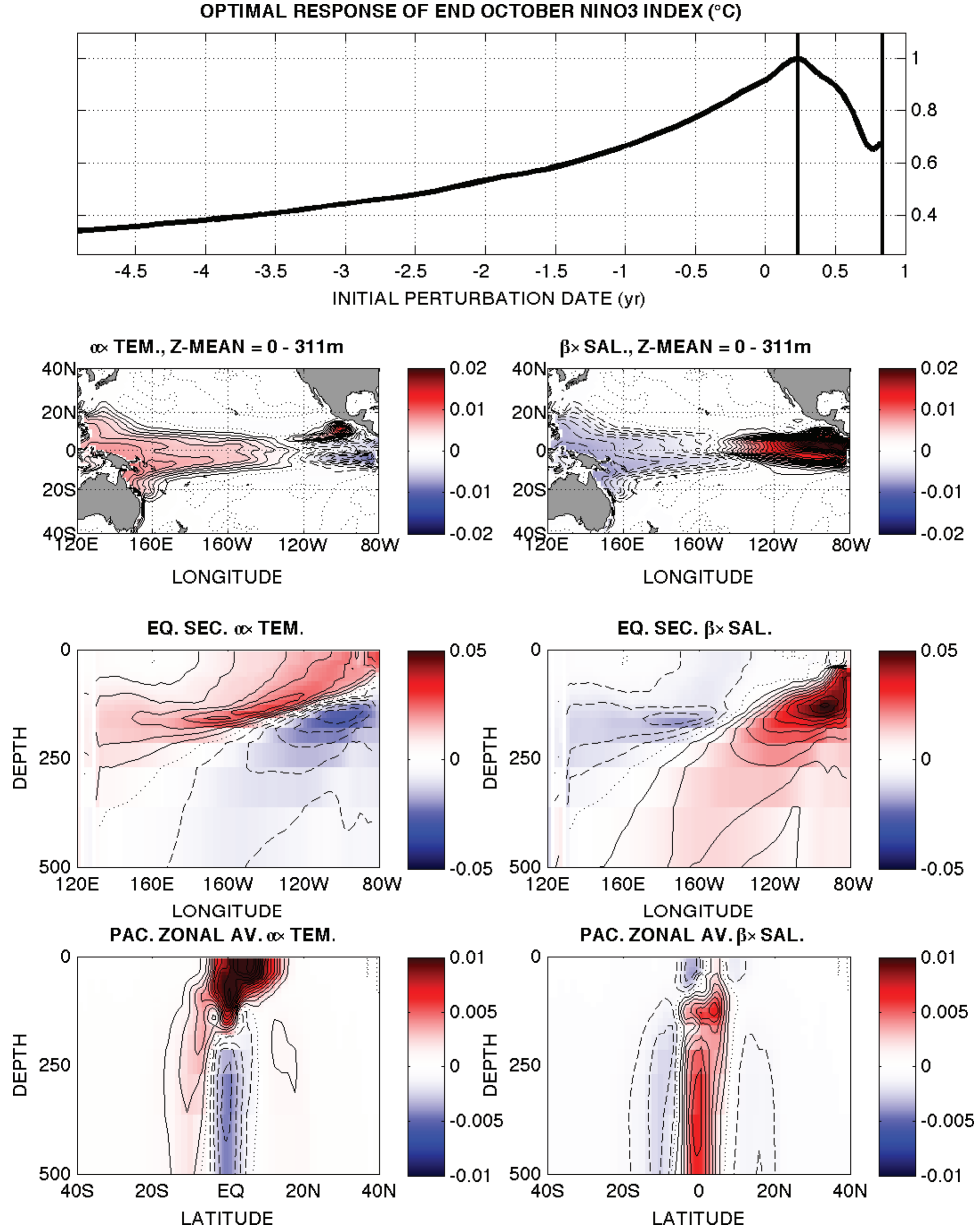**OPTIMAL RESPONSE OF END OCTOBER NINO3 INDEX (°C)**

Figure 5. The Nino3 SST index and the structure of the optimal initial anomalies for the maximization time (t_m) set in October. (Top panel) the magnitude of the Nino3 index in October as a function of the time (t_i) when the optimal perturbation was applied. (i.e., a transect of Fig. 4 along the vertical axis for the October 31st as maximization date, t_m). The time delay ($t_m - t_i$) that leads to the strongest transient growth is indicated by the vertical lines. The initial perturbations have been rescaled to lead to a 1°C change in the Nino3 index. (Middle and bottom panels) the optimal initial anomalies in temperature and salinity, shown in term of density (kg m^{-3}), for the delay time causing the strongest growth in the top panel. From top to bottom: temperature and salinity anomalies averaged from the surface to 311 m, anomalies along the equator, and zonally-averaged values. Solid, dashed and dotted lines correspond to positive, negative and zero values, respectively. Contour intervals are 1×10^{-3} or 5×10^{-3} kg m^{-3} for the equatorial section.

and maximization times, t_m, from the end of October to the end of January (these particular dates correspond to the local maximum in Fig. 4 with the values of the Nino3 SST response above 0.975°C). On average, SST increase for other dates is 20 to 30% smaller. In other words, the SSTs of the eastern equatorial Pacific during the three months at the end of the calendar year are most sensitive to a 20-day interval at the beginning of April.

Another interpretation of this result is that the initial date of the optimal perturbation strongly affects how long the transient growth should continue to achieve the strongest response. For instance, the strongest transient growth of the optimal solution with the initialization at the end of March is achieved after 220 days, whereas for initialization in mid-April the time delay (i.e., $\tau = t_m - t_i$) will be 290 days (Fig. 4).

To understand these findings, we will next focus on two different "experiments." The first experiment corresponds to the most efficient optimal perturbation we have found: the one with the initial time at the end of March and the final date at the end of October (the maximization interval, τ, of 220 days). This experiment will be called the October experiment ($|\boldsymbol{u}^{\text{Oct}}(t)\rangle =| \boldsymbol{u}^{\text{opt}}_{\{t_i,t_m\}}(t)\rangle|_{\text{Oct}}$). The other experiment will be a more conventional case with the initial date on April 5$^{\text{th}}$ and the final date at the end of December ($|\boldsymbol{u}^{\text{Dec}}(t)\rangle = |\boldsymbol{u}^{\text{opt}}_{\{t_i,t_m\}}(t)\rangle|_{\text{Dec}}$). This experiment will be called the December experiment (the maximization interval of 270 days).

b. Optimal growth

i. The structure of the optimal perturbations. The optimal initial perturbations for the two experiments (October and December) are very similar and are dominated by salinity which contributes nearly ~65% to the norm $\langle \boldsymbol{u}^{\text{opt}}(t_i)|\mathbf{N}|\boldsymbol{u}^{\text{opt}}(t_i)\rangle$, while the rest is due to temperature. Both temperature and salinity anomalies modify the density field to induce an east-west gradient of density (Fig. 5, middle panel). Even though this gradient is positive at the ocean surface, the depth-integrated density gradient is negative, which corresponds to the deepening of the pycnocline in the western part of the basin and a shoaling in the east (equivalent to an increase in the slope of the pycnocline along the equator). The meridional structure of perturbations in both experiments is nearly symmetric about the equator (Fig. 5, bottom panels).

The similarity of the two optimal initial perturbations can be verified by calculating the norm-like product of the perturbations $\langle \boldsymbol{u}^{\text{Dec}}(t_i)|\mathbf{N}|\boldsymbol{u}^{\text{Oct}}(t_i)\rangle = 0.96$ which is very close to unity (note that $\langle \boldsymbol{u}(t_i)|\mathbf{N}|\boldsymbol{u}(t_i)\rangle = 1$ by the definition of the optimal solutions). This result confirms that the structures of initial anomalies for the two cases are very similar and hence any difference between the growth timescales should be set by the seasonally-varying ocean basic state.

When the two solutions reach their maxima (in terms of the Nino3 index - Fig. 6, top panel), the structures of the anomalies still remain very close (even the maxima are achieved in different months of the seasonal cycle; i.e., in October and December). Again, calculating the norm-like product between those anomalies gives
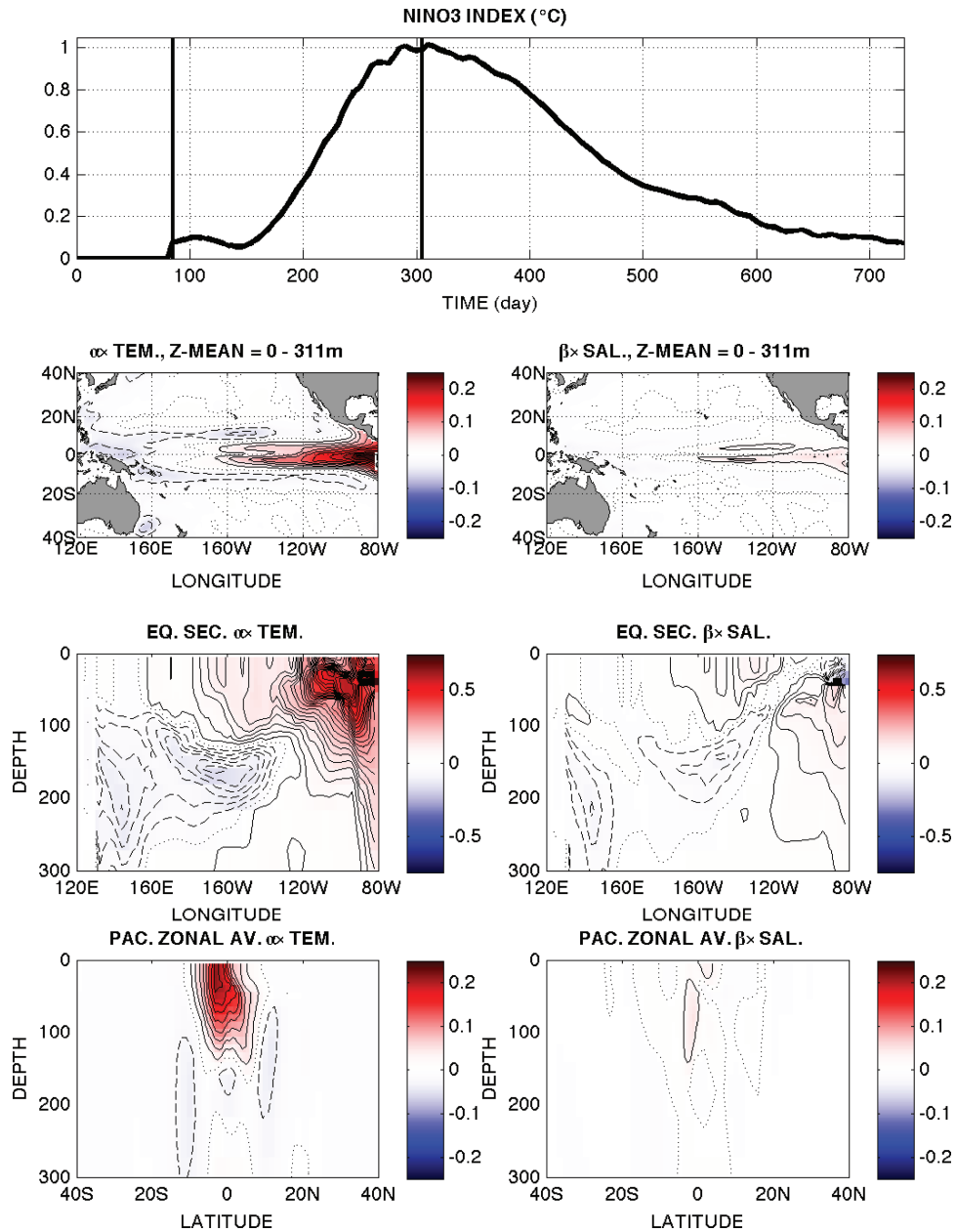
Figure 6. Integration of the tangent linear (forward) model from t_i (March 26th) to t_m (October 31st) with the initial conditions given by the optimal perturbation. (Top panel) the Nino3 SST index as a function of time. The initial date and the date when the index reaches its maximum are indicated by two vertical lines. (Middle and bottom panels) the temperature (left) and salinity (right) fields in terms of density, in $kg\,m^{-3}$, at the peak of the Nino3 index. From top to bottom: temperature and salinity anomalies averaged from the surface to 311 m, anomalies along the equator, and zonally-averaged anomalies. Solid, dashed and dotted lines correspond to positive, negative and zero values, respectively. Contour intervals are $2.5 \times 10^{-2}\,kg\,m^{-3}$. Note that now it is temperature that predominantly controls density.

$$\frac{\langle \boldsymbol{u}^{\text{Dec}}(t_m)|\mathbf{N}|\boldsymbol{u}^{\text{Oct}}(t_m)\rangle}{\sqrt{\langle \boldsymbol{u}^{\text{Dec}}(t_m)|\mathbf{N}|\boldsymbol{u}^{\text{Dec}}(t_m)\rangle \langle \boldsymbol{u}^{\text{Oct}}(t_m)|\mathbf{N}|\boldsymbol{u}^{\text{Oct}}(t_m)\rangle}} = 0.94.$$

It is critical that by the time of the maximum SST response, the two solutions become strongly dominated by temperature (αT is an order of magnitude greater than βS). In fact, the optimal solutions develop a strong positive temperature anomaly in the eastern equatorial Pacific in the top 100–200 m of the ocean, which is largely symmetric about the equator (Fig. 6). The difference between the maxima of the Nino3 index for the two cases, calculated as $\langle \boldsymbol{F}|\boldsymbol{u}^{\text{Dec}}(t_m)\rangle$ and $\langle \boldsymbol{F}|\boldsymbol{u}^{\text{Oct}}(t_m)\rangle$, is less than 2%.

We have tested other optimal perturbations initiated between mid-March and the end of April, and they all looked very similar to those we just described. This confirms that the differences in the transient growth timescale do not come from the structure of the optimal perturbations but rather from the annual trajectory of the system (i.e., the state of the ocean when the perturbation is imposed). Hereafter, to understand physical mechanisms leading to the transient growth, we will focus on the October experiment, since it produces the greatest warming of the Nino3 SSTs. We stress, however, that differences between the solutions reaching their maxima in October and December are minor.

ii. The mechanisms of the optimal growth. After the optimal initial perturbations in temperature and salinity are imposed, a gradual adjustment of the ocean follows. It is this adjustment that leads to the transient warming of the eastern equatorial Pacific. The entire process can be divided into three phases: a quick local adjustment of the salinity dominated anomalies ($\sim$1 months), the large-scale equatorial basin adjustment (2 to 9 months), and the gradual decay of the anomaly (Fig. 6, top panel, and Figs. 7 and 8).

Phase 1: During the first few weeks after t_i, the velocities adjust to the initial temperature-salinity anomaly (seen in Fig. 8 as an increase of the second order kinetic energy in the system $- \iiint dv\, u^2 + v^2$, where u and v are the anomalous zonal and meridional velocity, respectively). Several separate Kelvin waves of opposite signs are excited from different locations along the equator (e.g., Fedorov and Brown, 2009). The off-equatorial anomalies are feeding onto the equator in the western Pacific, which leads to the accumulation of heat and deepening of the thermocline there. This is followed by a slight increase in the system anomalous potential energy (Fig. 8).

The initial deepening of the thermocline in the western equatorial Pacific and the resulting potential energy increase are induced by both salinity and temperature components of the initial anomalies. To demonstrate this, we have performed two time integrations imposing only temperature or salinity component of the initial perturbation (Fig. 8). It is significant that, even without temperature, the salinity anomaly is able to deepen of the pycnocline and induce a positive temperature anomaly at the base of the pycnocline, which will initiate the transient growth of the Nino3 index. However, the result is greater when both components are present in the initial condition.
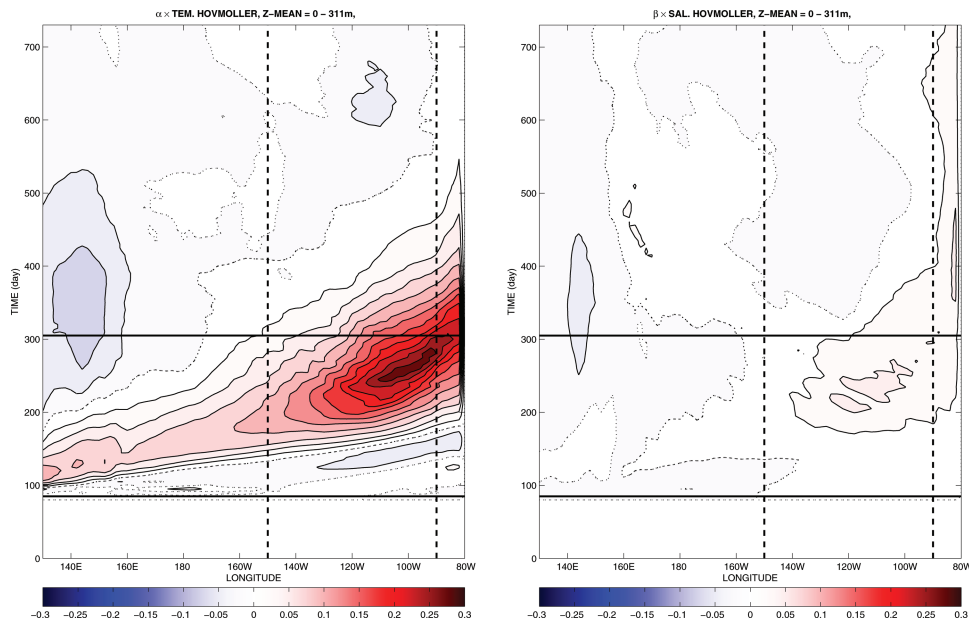
Figure 7. Hovmöller diagrams for anomalies in (left) temperature and (right) salinity along the equator, shown in terms of density (kg m^{-3}) and averaged over the upper 311 m obtained by direct integrations of the tangent linear (forward) model. The anomalies are excited by the optimal perturbations in temperature and salinity. The horizontal lines denote the initial perturbation date and the date when the Nino3 SST index reaches its maximum. Solid, dashed and dotted lines correspond to positive, negative and zero values, respectively. Contour intervals are 2.5×10^{-2} kg m^{-3}.

Phase 2: At the beginning of phase 2 a strong Kelvin wave is excited from the western equatorial Pacific (induced by the deepening of the pycnocline that had occurred in the west during phase 1). When this downwelling Kelvin wave reaches the eastern Pacific in about 2-3 months (Fig. 7), it establishes a large-scale anomaly in the east-west temperature gradient along the equator (it is relatively weak at first), initiates the warming of SSTs in the east, and sets up the stage for more warming. However, had it been just for this Kelvin wave, the warming in the east would be relatively weak and short lasting.

Yet, the thermocline in the eastern equatorial Pacific continues to deepen and temperature in the eastern Pacific continues to increase, which further reduces the temperature gradient along the equator. This phase of the ocean adjustment is controlled by two complimentary processes: (i) the generation of a basin-wide cyclonic Rossby wave that slowly propagates westward and (ii) the excitation of a continuum of downwelling Kelvin waves along the equator.

The Rossby wave helps sustain a large-scale anomalous eastward current along the equator (Figs. 9 and 10). This nearly geostrophic (except in the vicinity of the equator) current
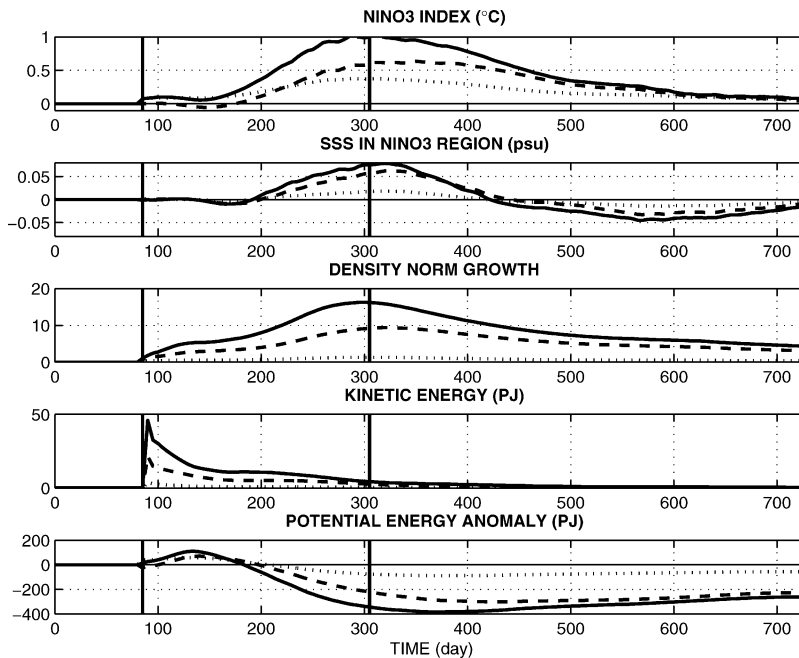
Figure 8. Several diagnostics from the integration of the tangent linear model with the initial conditions given by the optimal perturbation. From top to bottom: the Nino3 index, the sea surface salinity in the Nino3 region, the nondimensional density norm growth, the second order kinetic energy, and the potential energy anomaly (the latter two variables are averages over the full ocean). Solid, dashed and dotted lines correspond to the combined temperature-salinity initial perturbation, the salinity-only perturbation, and the temperature-only perturbation, respectively. The vertical lines denote the initial perturbation date and the date when the Nino3 index reaches its maximum.

leads to a persistent anomalous zonal advection of warm water from the west to the east and, consequently, a significant warming of the Nino3 SST. The continuum of downwelling Kelvin waves deepens the thermocline in the east (Fig. 7) and also contributes to the anomalous zonal flow (Fig. 9). The constructive effect of the two aforementioned processes sets the intensity and duration of the transient growth. In particular, the relatively long time scale of the Rossby wave propagation and the related persistence of anomalous advection prolong the transient growth time (by 220 days for the October experiment, Fig. 7).

The transient growth of the temperature anomaly in the east is linked to the non-normality of the ocean dynamics related to the propagation of Kelvin and Rossby waves and to zonal advection (see Section 4). The non-normality leads to a strong increase of the temperature-salinity norm during the growth phase: $\langle \boldsymbol{u}(t_m)|\mathbf{N}|\boldsymbol{u}(t_m)\rangle/\langle \boldsymbol{u}(t_i)|\mathbf{N}|\boldsymbol{u}(t_i)\rangle > 15$, (see Fig. 8). This norm increase highlights the role of non-normal processes in the transient growth (Farrell, 1988). In fact, although *a priori* our analysis was aimed at maximizing a linear cost function (not a norm of the perturbations), the non-normality becomes critical.
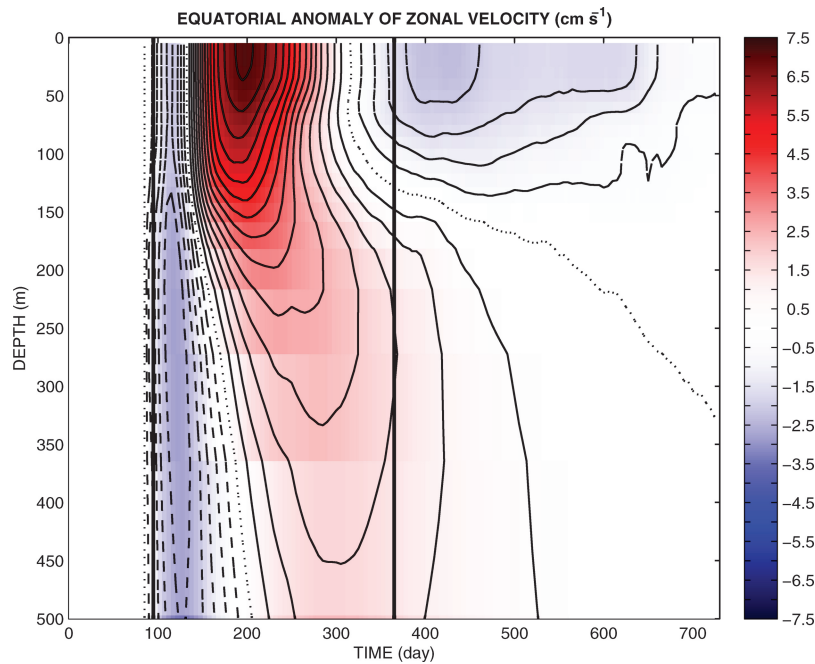
EQUATORIAL ANOMALY OF ZONAL VELOCITY (cm s⁻¹)

Figure 9. A Hovmöller-like diagram for the anomalous (zonally-averaged) eastward velocity along the equator (cm s^{-1}) as a function of time and depth. The anomalous eastward flow is induced by the initial optimal perturbations in temperature and salinity. The vertical lines denote the perturbation date and the date when the Nino3 index reaches its maximum. Solid, dashed and dotted lines correspond to positive, negative and zero values, respectively. Contour intervals are 0.5 cm s^{-1}.

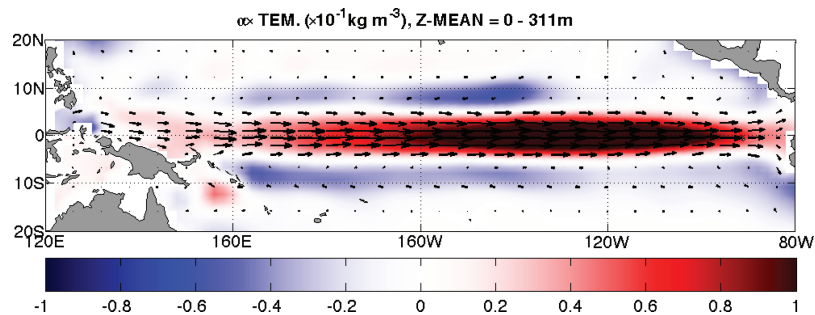**∝ TEM. (×10⁻¹ kg m⁻³), Z-MEAN = 0 - 311m**

Figure 10. Anomalies in temperature (color) and velocity (arrows) averaged over the top 310 m at the time when the anomalous eastward flow reaches its maximum (110 days after the perturbations were imposed, see Fig. 9). The meridional structure of the temperature field resembles that of a superposition of basin-wide downwelling Kelvin and upwelling Rossby waves that control the nearly geostrophic eastward flow along the equator. The current intensifies towards the equator where the Coriolis parameter vanishes: right at the equator the flow velocity is limited by friction. The largest arrows correspond to velocity 6.7 cm s^{-1} (after depth averaging). The actual velocity can reach 14.6 cm s^{-1}.

Phase 3: The last phase of the ocean adjustment begins after the anomalous zonal advection reverses its direction (Fig. 9). This reversal, together with other processes such as coastal Kelvin waves, allows the eastern Pacific to gradually cool to its seasonal values. A gradual ocean adjustment continues for a while as highlighted by the slow evolution of potential energy of the basin (Fig. 8).

As one would expect for optimal perturbations, the transient increase in temperature of the eastern equatorial Pacific is achieved by the constructive effect of the whole perturbation. The large meridional and depth extent of the initial anomalies (roughly from 20°S to 20°N and from the surface to about 500 m) is critical for generating the warming in the east. In other words, there exists a focusing effect by which basin-scale anomalies in temperature and salinity produce a strong warming in a relatively confined Nino3 region.

To illustrate this idea and explore which spatial segments of the initial anomaly are most effective in changing the Nino3 index, we split the basin into six sub-domains using two latitude lines (5°N and 5°S) and one meridian (160°W) as the boundaries (Fig. 11, top panel). We then conducted six experiments with the tangent linear (forward) model, each time retaining initial anomalies only in one of the sub-domains and setting the rest to zero. For simplicity, we explored the temperature-only perturbations.

The evolution of the Nino3 SST for these six experiments is shown in Figure 11, bottom panel. Contributions to the transient growth are almost equally spread between five regions (the Eastern-Equatorial subdomain provides the largest contribution, while the Southeastern domain has virtually no effect). Despite the growth is achieved by equatorial wave dynamics, these experiments highlights the constructive effect of these waves stimulated all over the equatorial region. This shows that even though the equatorial wave dynamics is obviously critical for the transient growth, almost the entire tropical region participates in the adjustment of the equatorial ocean. These experiments also emphasize the role of the basin-scale Rossby waves that control the adjustment outside of the narrow equatorial strip.

4. An idealized model for the transient growth

In order to better understand the mechanisms of the transient warming, here we consider a highly idealized model of the tropical ocean dynamics capable of undergoing a similar optimal transient growth. To that end, we restrict the dynamics to the mechanisms highlighted in Section 3: the eastward propagation of temperature anomalies, the ability of anomalous zonal advection to extract heat from the ocean background state, and the damping of temperature by slow processes. The model will describe changes in the ocean heat content along the equator as

$$\partial_t T_E = -u \frac{\Delta \overline{T}}{L} + \omega T_W - r T_E, \tag{10}$$

$$\partial_t T_W = +u \frac{\Delta \overline{T}}{L} - \omega T_W - r T_W, \tag{11}$$

EXPERIENCES BOUNDARIES
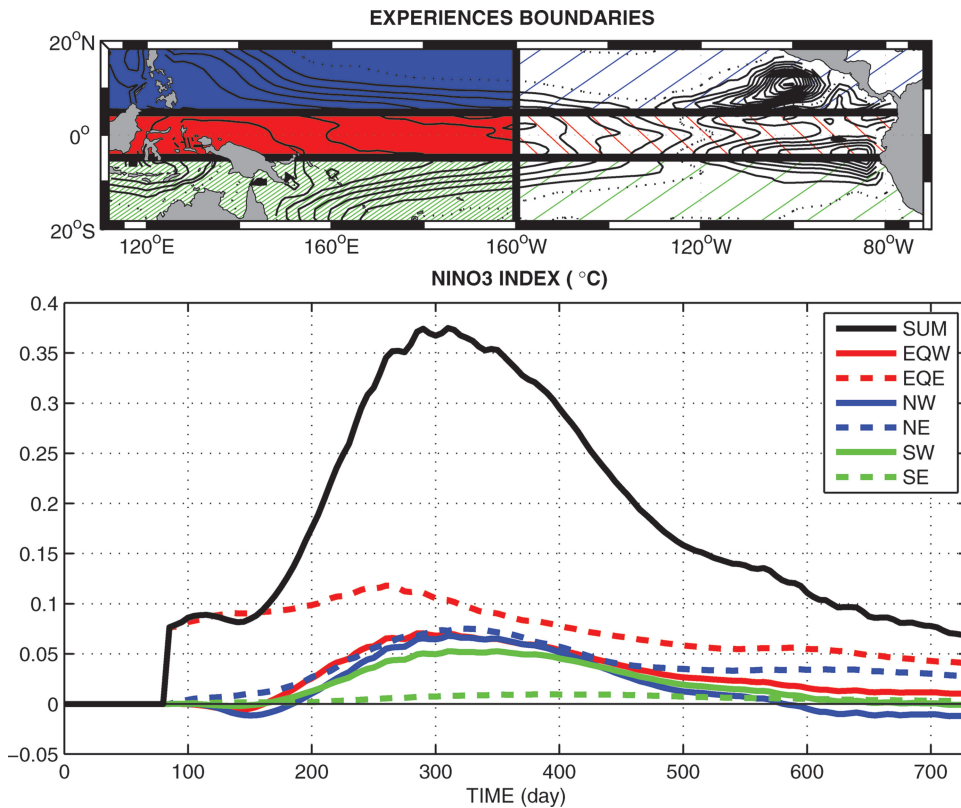

NINO3 INDEX (°C)

Figure 11. The focusing effect: (top) splitting the ocean basin into six sub-domains. The separating lines are the 160°W meridian and the 5°S and 5°N latitudes. (Bottom) the evolution of the Nino3 SST index in each of the six temperature-only experiments, in which initial temperature anomalies are retained only in the respective sub-domains. The black line indicates SST changes when the full temperature perturbation is imposed.

where T_E and T_W are anomalies of the ocean heat content in two boxes corresponding to the eastern and western equatorial Pacific, respectively (here ocean heat content is defined as temperature averaged over the upper 350 m - the depth of anomalies in the GCM, see Fig 6 and 9). We will refer to T_E and T_W as the east and west temperatures. For simplicity, salinity variations, the seasonal cycle and Rossby waves are neglected. Note that this system is similar to an SST equation used in the theory of ENSO where only two key feedbacks (thermocline and zonal advection) are taken into account; e.g., Fedorov and Philander (2001).

The anomalous advection of the mean temperature gradient is described by u - the anomalous zonal velocity, $\Delta\overline{T}$ - the east-west difference in ocean heat content associated with the mean zonal temperature gradient, and L - the distance between the east and west boxes.

Table 1. Parameters used for the idealized model in Section 4 and the Appendix.

k	$1/12°\text{C}^{-1}\,\text{month}^{-1}$	The proportionality coefficient (for zonal advection)
a	$2/3$	East weight coefficient (for zonal advection)
b	$1/3$	West weight coefficient (for zonal advection)
ω	$1/3\,\text{month}^{-1}$	Inverted Kelvin wave time scale
r	$1/24\,\text{month}^{-1}$	Oceanic damping rate
$\Delta\overline{T}$	$-6°\text{C}$	Mean east-west temperature difference
$\Delta\overline{T}_V$	$20°\text{C}$	Mean temperature difference across the thermocline
H	$350\,\text{m}$	Depth of the equatorial boxes
h	$150\,\text{m}$	Mean thermocline depth
L	$10^7\,\text{m}$	Distance between the east and west boxes
α	$2.5 \times 10^{-4}°\text{C}^{-1}$	Thermal expansion coefficient

The terms proportional to ω characterize the eastward propagation of heat content anomalies by equatorial Kelvin waves. Finally, r is the oceanic damping rate representing various dissipative processes (coastal Kelvin waves, friction, etc.). Adding Eqs. (10) and (11) yields a simple constraint that the net anomalous heat content of the equatorial ocean, $T_E + T_W$, should decay with an e-folding time scale of $1/r$.

We now assume that anomalies in the zonal velocity are proportional to a weighted sum of anomalies in the east and west ocean heat contents; that is, $u = kL(aT_E + bT_W)$ with a larger weight given to T_E ($a > b$). This approximation implies that a deepening of the equatorial thermocline in the east is associated with an eastward anomaly in the zonal velocity. Such a simple relationship between u and $aT_E + bT_W$ is obviously an idealization, but it allows us to introduce a dependence of zonal velocity on the changing state of the ocean (for details see the Appendix). All relevant parameters and their values in this study are summarized in Table 1.

Eqs. (10) and (11) can be rewritten as:

$$\partial_t \begin{pmatrix} T_E \\ T_w \end{pmatrix} = \begin{pmatrix} -ak\Delta\overline{T} - r & -bk\Delta\overline{T} + \omega \\ +ak\Delta\overline{T} & +bk\Delta\overline{T} - \omega - r \end{pmatrix} \begin{pmatrix} T_E \\ T_W \end{pmatrix}. \tag{12}$$

A linear stability analysis for Eqs. (12) gives two egeinvalues

$$\begin{cases} \lambda_+ = -r, \\ \lambda_- = (b - a)k\Delta\overline{T} - \omega - r. \end{cases}$$

When $\lambda_- < 0$, the system is damped and any perturbation must decay eventually. Since r and ω are positive, Kelvin wave dynamics and oceanic damping have a stabilizing effect on the egeinvalues. The system stability is thus determined by the constraint: $(b-a)k\Delta\overline{T} < \omega + r$, which is satisfied for our set of model parameters (Table 1).

The two eigenvectors associated with these eigenvalues are:

$$|\boldsymbol{u}_+\rangle = [\,\omega + (a-b)k\Delta\overline{T}]^{-\frac{1}{2}}\begin{pmatrix}\omega - bk\Delta\overline{T}\\ ak\Delta\overline{T}\end{pmatrix}, \text{ and } |\boldsymbol{u}_-\rangle = [\,\omega + (a-b)k\Delta\overline{T}]^{-\frac{1}{2}}\begin{pmatrix}-1\\ +1\end{pmatrix}.$$

Their associated biorthogonals (i.e., the eigenvectors of the adjoint problem) are

$$\left|\boldsymbol{u}_+^\dagger\right\rangle = [\omega + (a-b)k\Delta\overline{T}]^{-\frac{1}{2}}\begin{pmatrix}+1\\ +1\end{pmatrix}, \text{ and } \left|\boldsymbol{u}_-^\dagger\right\rangle = [\omega + (a-b)k\Delta\overline{T}]^{-\frac{1}{2}}\begin{pmatrix}-ak\Delta\overline{T}\\ \omega - bk\Delta\overline{T}\end{pmatrix}.$$

Since the eigenvectors (and their biothogonals) are not orthogonal, the idealized model is non-normal and both Kelvin wave propagation and zonal advection contribute to the non-normality. For the former effect, the non-normality is related to the fact that Kelvin waves can propagate only eastward. For the latter, the non-normality is related to the dependence of anomalous zonal advection on temperature anomalies. If one sets $\omega = 0$ (with $a \neq b$) or $k = 0$, the system still remains non-normal and its eigenvectors not orthogonal. If both ω and k are set to zero, then Eqs. (12) have only one degenerate eigenvalue $\lambda_\pm = -r$.

The non-normal character of the system suggests a possibility of a transient growth associated with Kelvin wave propagation and zonal advection. Using the eigenvectors and their biorthogonals we obtain the solutions of this idealized model as:

$$\begin{pmatrix}T_E(t)\\ T_W(t)\end{pmatrix} = \left(|\boldsymbol{u}_+\rangle e^{\lambda_+ t}\langle\boldsymbol{u}_+^\dagger| + |\boldsymbol{u}_+\rangle e^{\lambda_- t}\langle\boldsymbol{u}_+^\dagger|\right)\begin{pmatrix}T_E(0)\\ T_W(0)\end{pmatrix},$$

$$= \omega^{-1}\left[\begin{pmatrix}\omega - bk\Delta\overline{T}\\ ak\Delta\overline{T}\end{pmatrix}e^{-rt}(+1, +1)\right.$$

$$\left. + \begin{pmatrix}-1\\ +1\end{pmatrix}e^{-(\omega+r)t}(-ak\Delta\overline{T}, \omega - bk\Delta\overline{T})\right]\begin{pmatrix}T_E(0)\\ T_W(0)\end{pmatrix}. \tag{13}$$

Choosing the east temperature T_E as the coast function, $\langle\boldsymbol{F}| = (1, 0)$, and the sum of the squares of the east and west temperatures, $T_E^2 + T_W^2$, as the norm (with $\mathbf{S} = \mathbf{I}$), we apply the general expression for the optimal perturbations (8) to obtain the optimal initial anomalies for our idealized model. For simplicity, we use the asymptotic limit of large delay and obtain the optimal initial perturbation:

$$\begin{pmatrix}T_E^{\text{opt}}\\ T_W^{\text{opt}}\end{pmatrix} = \frac{c}{\sqrt{2}}\begin{pmatrix}+1\\ +1\end{pmatrix}, \tag{14}$$

where the constant c is set to 0.4, yielding the maximum increase in Nino3 index of $1°C$ (for the set of model parameters corresponding to $\Delta\overline{T} = -6°C$, see Table 1).

Using this perturbation as the initial condition for the idealized model we obtain an expression for the optimal evolution of the east temperature as a function of time:

$$T_E^{\text{opt}}(t) = \frac{c}{\sqrt{2}}\frac{2(\omega - bk\Delta\overline{T})e^{-rt} - [\omega - (a+b)k\Delta\overline{T}]e^{-[(a-b)k\Delta\overline{T}+\omega+r]t}}{\omega + (a-b)k\Delta\overline{T}}. \tag{15}$$
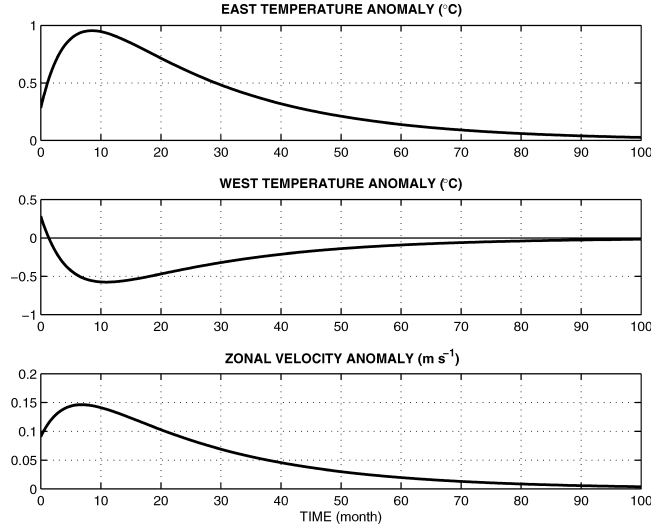
Figure 12. Transient growth in the idealized model: (top) the east temperature anomaly, (middle) the west temperature anomaly, °C, and (bottom) the zonal velocity anomaly, m s^{-1} as a function of time.

This expression shows a strong transient increase of the east temperature in a few-month time (Fig. 12). From Eq. (15) we calculate the time $t_{\max}$ when the east temperature reaches its maximum (i.e., the growth time) as

$$t_{\max} = \frac{1}{\omega + (a - b)k\Delta\overline{T}} \log\left(\frac{[(a - b)k\Delta\overline{T} + \omega + r][\omega - (a + b)k\Delta\overline{T}]}{2r(\omega - bk\Delta\overline{T})}\right). \qquad (16)$$

Substituting typical ocean parameters from Table 1 into (16) gives $t_{\max} = 8.6$ months, which falls in the range of the GCM experiments (between 7.3 and 9 months). The non-normality of the system evolution is apparent in the norm's transient increase

$$[T_E^2(t_{\max}) + T_W^2(t_{\max})]/[T_E^2(0) + T_W^2(0)] > 7.$$

The transient growth (with temperature increasing in the east and decreasing in the west) is related to both the eastward Kelvin wave propagation and zonal advection of the mean temperature, which is similar to the optimal growth in our GCM experiments. If one neglected the advection contributions to (16), i.e., set $k = 0$ or $\Delta\overline{T} = 0$, he or she would obtain

$$t_{\max} = \frac{1}{\omega} \log\left(\frac{\omega + r}{2r}\right). \qquad (17)$$

This gives a significantly shorter growth time $t_{\max} = 4.5$ months, which is just slightly longer than the time needed for a Kelvin wave to cross the Pacific basin.

MAXIMUM TIME DELAY (month)

MEAN TEMPERATURE DIFFERENCE (°C)

MAXIMUM EAST TEMPERATURE ANOMALY (°C)
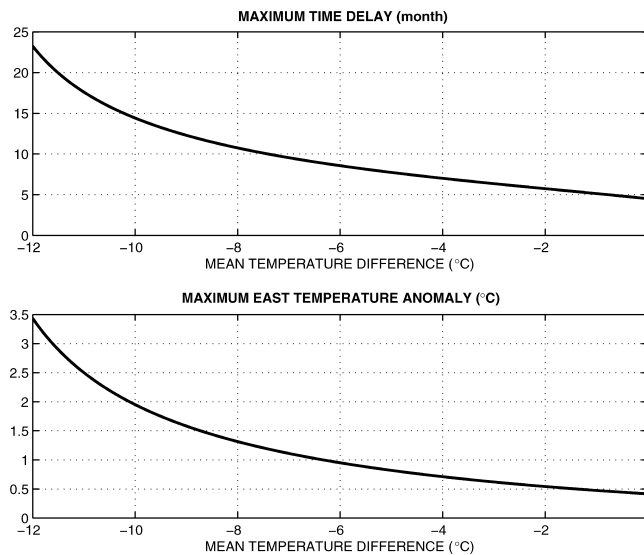
MEAN TEMPERATURE DIFFERENCE (°C)

Figure 13. (Top) the time of the transient growth for the optimal solution, i.e., $t_m - t_i$, and (bottom) the maximum amplitude of the east temperature anomaly, in °C (see Fig. 12), as a function of the mean east-west temperature contrast in the idealized model. The graphs indicate that the zonal advection feedback (proportional to the mean zonal temperature difference) lengthens the growth time (delay) and amplify the warming in the eastern equatorial Pacific.

From expressions (15) and (16) we can calculate the growth time $t_{\max}$ and the magnitude of the transient increase in the east temperature $T_E^{\mathrm{opt}}(t_{\max})$ as a function of the mean east-west temperature contrast $\Delta \overline{T}$ (Fig. 13).

The results of Figure 13 are central for our study as they show that the zonal advection feedback is indeed critical for the transient growth. A stronger mean east-west temperature contrast, and hence a stronger advection feedback, amplifies the Nino3 SST response (from 0.5°C to several degrees) and at the same time prolongs the growth time significantly (from 4 months to a year or possibly longer).

Extrapolating these results to the case of the annual cycle (which modifies the temperature gradient $\Delta \overline{T}$) is not straightforward. However, it appears that the heat content of the Western Pacific warm pool and conditions for eastward anomalous advection are critical. In the ocean GCM, the strongest warm pool develops in March-April (Fig. 3) with the maximum reached around the Equinox (April 15th, Fig. 14, top panel). Additionally, around this time the mean easterly winds relax decreasing the surface westward velocity in the ocean (Fig. 14, bottom panel), creating favorable conditions for the anomalous eastward advection. This is exactly the period that the adjoint model indicates as the most sensitive interval for perturbations to induce a strong response in the Nino3 index (Fig. 4).

In summary, the idealized model illustrates the key mechanisms of the transient (non-normal) SST growth in the eastern Pacific related to the Kelvin wave propagation and
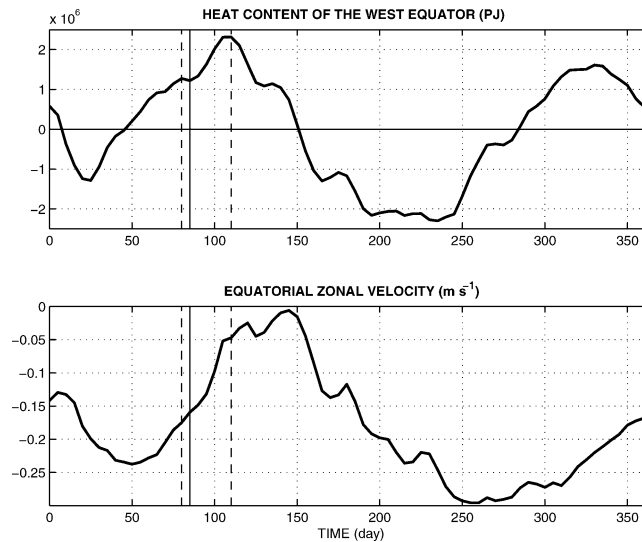
Figure 14. (Top) seasonal changes in the heat content of the ocean warm pool in the western equatorial Pacific (integrated between 5°S to 5°N and 140°E to 180°E, and from the surface to 310 m) as simulated by the GCM. (Bottom) seasonal changes in the (zonally-averaged) zonal velocity along the equator over the Pacific (integrated from surface to 50 m) as simulated by the GCM. The two vertical dashed lines indicate the period of the year when imposing optimal perturbations would influence the Nino3 SST index by the end of the year most (see Fig. 4). The solid vertical line denotes March 26th - the very best optimal initial date for perturbing this index in the model.

anomalous eastward advection. The advection term increases the amplitude of the transient growth and lengthens the growth time. The idealized model also provides tentative clues for why the system is most sensitive (in terms of subsequent changes in the Nino3 index) to perturbations around the time of the Equinox.

5. Discussion and conclusions

The focus of this study is the sensitivity of sea-surface temperature in the eastern equatorial Pacific (the Nino3 region) to large-scale temperature and salinity perturbations within an ocean-only approach. Using the generalized stability analysis of an ocean GCM (OPA 8.2), we have computed optimal initial perturbations (in salinity, temperature, or both) that induce a strong transient growth of the Nino3 SST index. To illustrate key ideas of the study, we have formulated a simple model of the ocean dynamics in the equatorial Pacific that capture the main mechanisms of the transient growth.

The structure of the optimal initial anomalies is characterized by large-scale zonal gradients of temperature and salinity that create an anomalous density gradient along the equator (initially corresponding to a greater east-west slope of the pycnocline). The anomalies are

localized in the upper 500 m along the equatorial strip between 10°S–10°N, but extend
to 20°S/N in the western Pacific. An important feature of the anomalies is a pronounced
warming and freshening of the western Pacific, which is largely symmetric with respect to
the equator.

The off-equatorial changes in temperature and salinity are important elements of the
optimal perturbations that can feed onto the equator and then amplify and prolong the
transient growth. In fact, there occurs a focusing effect by which different parts of the initial
anomalies (some quite far away from the equator) ultimately contribute to a temperature
increase in the limited area of the eastern equatorial Pacific.

The optimal perturbations induce a strong transient growth of the Nino3 SST that reaches
its maximum amplitude 7 to 9 months after the initial conditions were imposed. The transient
growth is very efficient - an initial anomaly with zonal contrasts in temperature and salinity
of 0.15 psu and 0.25°C leads to a 4°C warming of the Nino3 index. Taken separately, such
perturbations in the salinity or temperature fields would still lead to a significant increase
in the Nino3 index (2.5°C or 1.5°C, respectively).

As clear from the idealized model, the origin of the transient growth is the non-normality
of ocean dynamics related to the eastward propagation of equatorial Kelvin waves and the
anomalous zonal advection of mean temperature. This zonal advection feedback strengthens
the amplitude and extends the duration of the transient growth (the strength of the feedback
depends on the mean east-west temperature contrast along the equator). The anomalous
zonal flow along the equator is associated in part with a basin-wide cyclonic Rossby wave
that gradually propagates westward along the equator as part of the ocean adjustment. This
anomalous eastward flow, together with a continuum of Kelvin waves, leads to a strong
warming of the eastern equatorial Pacific and a flattening of the equatorial thermocline (as
seen in the reduction of the ocean potential energy, for example). In due time, the anomalous
zonal advection reverses, the transient growth stops and the system gradually returns to its
basic state (after 1–1.5 year or so).

In our experiments salinity anomalies appear to be an efficient trigger for subsequent
changes in the Nino3 index. Just after the first 2–3 months, the initial salinity perturbation
induces a large-scale temperature anomaly that will control the further evolution of the
temperature and density fields. However, while important, salinity is not critical for the
optimal growth - a transient growth does occur without salinity both in the ocean OGCM
and the idealized model. Moreover, since the basic state of the ocean has a rather weak
mean salinity gradient along the equator, an advection feedback involving the mean salinity
gradient would be negligible.

Our analysis shows the importance of seasonal ocean conditions between the end of March
and mid-April for the evolution of the optimal perturbations. This interval corresponds to
the Equinox when the ocean warm pool reaches its maximum heat content (April 15th)
while the easterly winds become relaxed, as compared to mean values. The large heat
content of the western equatorial Pacific and the relaxed winds during the Equinox allow
for a stronger anomalous eastward advection of heat, which results in a particularly strong

transient warming in the eastern equatorial Pacific. This enhanced sensitivity of the ocean during the spring and the subsequent increase of temperature in the east by the end of the calendar year resemble the phase-locking of El Niño-Southern Oscillation (ENSO) to the seasonal cycle. On the other hand, such enhanced sensitivity can contribute to the Spring predictability barrier - potential errors in the system (or noise) projecting favorably onto the optimal initial perturbations can generate transient SST anomalies in the eastern Pacific that can interfere with El Niño prediction by hiding any prior precursor.

One important question that this work has not addressed is how the described transient growth is modified by ocean-atmosphere interactions. Clearly, the positive Bjerkness feedback can become important (warmer SSTs in the eastern equatorial Pacific lead to weaker zonal winds, deeper thermocline and even warmer SSTs; e.g., Fedorov and Philander, 2001). Thus, potentially the Bjerkness feedback can amplify the transient warming induced by optimal perturbations in exactly the same way that El Niño is amplified by the gradual weakening of easterly trade winds as part of the ENSO cycle. Incorporating this coupling between the ocean and the atmosphere will be a goal of the future work.

APPENDIX

Surface velocity and zonal temperature

In this Appendix, we will derive an approximate expression connecting anomalies in the zonal velocity and the equatorial temperature to be used in the idealized model. We will begin with a linear equation of state for seawater and the thermal wind balance:

$$\rho = \rho_0(1 - \alpha T), \tag{18a}$$

$$f\partial_z u = \frac{g}{\rho_0}\partial_y \rho, \tag{18b}$$

where ρ is density (ρ_0 is a constant reference density), α - the thermal expansion coefficient, T - temperature anomaly, g - the acceleration of gravity, f - Coriolis parameter, and u - anomaly in zonal velocity (also see Table 1). To avoid a singularity at the equator, we differentiate (18b) with respect to y, use the equatorial β-plane approximation ($f = \beta^* y$), and rewrite (18) as

$$\partial_z u = -\frac{g\alpha}{\beta^*}\partial_y^2 T, \tag{19}$$

which is valid in a close vicinity of the equator. Assuming that the flow is concentrated near the surface (above a depth H) and choosing the equatorial Rossby radius of deformation L_R

as the characteristic meridional scale (based on the phase speed of Kelvin waves propagating on the thermocline (of depth h), we approximate (19) as

$$u \simeq \frac{Hg\alpha}{\beta^* L_R^2} T, \quad \text{and} \quad L_R^2 = \frac{\sqrt{g^*h}}{\beta^*}, \tag{20}$$

where $g^* = g\Delta\bar{\rho}/\rho_0$ is the reduced gravity and $\Delta\overline{T}_V$ - the mean temperature difference across the thermocline, such that $g^* = g\alpha\Delta\overline{T}_V$ (note that $\Delta\overline{T}_V$ and $\Delta\overline{T}$ are not necessarily equal to each other). For typical ocean values (Table 1), the phase speed velocity of the equatorial Kelvin waves is roughly $\sim$2.7 m s^{-1}.

The assumption that the second derivative of T with respect to y on the right-hand-side of (19) is proportional to temperature itself is obviously a crude simplification, but it allows us to keep the idealized model as simple as possible. We then obtain a linear relation between anomaly in temperature and zonal velocity:

$$u \simeq kLT, \text{ with } k = \frac{H}{L}\sqrt{\frac{\alpha g}{h\Delta\overline{T}_V}}, \tag{21}$$

or for the two boxes (east and west) of the idealized model:

$$u_{E,W} \simeq kLT_{E,W},$$

where L is the zonal distance between the centers of the boxes and k is the coefficient of proportionality between temperature and zonal velocity.

We can now estimate the anomalous zonal flow between the two boxes as a weighted average of velocity in each box, i.e., as $u = au_E + bu_W$ or

$$u \simeq kL(aT_E + bT_W), \tag{22}$$

Substituting typical values of relevant parameters into (21) from Table 1 yields $k = 1/12°\text{C}^{-1}$ month^{-1}. Using different weights in (22) is not fundamental for the existence of the transient growth, but improves agreement with the GCM experiments.

REFERENCES

Arzel, O., T. Huck, and A. Colin de Verdière. 2006. The different nature of the interdecadal variability of the thermohaline circulation under mixed and flux boundary conditions. J. Phys. Oceanogr., *36*, 1703–1718.

Balmaseda, M. A., M. K. Davey, and D. L. T. Anderson. 1995. Decadal and seasonal dependence of ENSO prediction skill. J. Climate, *8*, 2705–2715.

Bjerknes, J. 1969. Atmospheric teleconnections from the equatorial Pacific. Mon. Wea. Rev., *97*, 163–172.

Blanke, B. and P. Delecluse. 1993. Variability of the tropical Atlantic Ocean simulated by a general circulation model with two different mixed-layer physics. J. Phys. Oceanogr., *23*, 1363–1388.

Blumenthal, B. 1991. Predictability of a coupled ocean-atmosphere model. J. Climate, *4*, 766–784.

Clarke, A. 2008. *An Introduction to the Dynamics of El Niño and the Southern Oscillation*, Academic Press, 308 pp.

Farrell, B. F. 1988. Optimal excitation of neutral Rossby waves. J. Atmos. Sci., *45*, 163–172.

Farrell, B. F. and P. J. Ioannou. 1996a. Generalized stability theory. Part I: Autonomous operators. J. Atmos. Sci., *35*, 2025–2040.

—— Ioannou. 1996b. Generalized stability theory. Part II: Nonautonomous operators. J. Atmos. Sci., *53*, 2041–2053.

Farrell, B. F. and A. M. Moore. 1992. An adjoint method for obtaining the most rapidly growing perturbation to oceanic flows. J. Phys. Oceanogr., *22*, 338–349.

Fedorov, A. V. 2010. Ocean response to wind variations, warm water volume, and simple models of ENSO in the low-frequency approximation. J. Climate, *23*, 3855–3873.

Fedorov, A. V. and J. Brown. 2009. Equatorial waves, *in* Encyclopedia of Ocean Sciences, 2nd ed., J. Steele, ed., Academic Press, 3679–3695.

Fedorov, A. V. and S. G. Philander. 2000. Is El Niño changing? Science, *288*, 1997–2002.

—— 2001. A stability analysis of the tropical ocean-atmosphere interactions: Bridging measurements of, and theory for, El Niño. J. Climate, *14*, 3086–3101.

Flügel, M. and P. Chang. 1999. Stochastically induced climate shift of El Niño-Southern Oscillation. Geophys. Res. Lett., *26*, 2473–2476.

Gent, P. R. and J. C. McWilliams. 1990. Isopycnal mixing in ocean circulation model. J. Phys. Oceanogr., *20*, 150–155.

Guilyardi, E., A. Wittenberg, A. V. Fedorov, M. Collins, C. Wang, A. Capotondi, G. J. van Oldenborgh, and T. Stockdale. 2009. Understanding El Niño in ocean-atmosphere general circulation models: Progress and challenges. Bull. Amer. Meteor. Soc., *90*, 325–340.

Huck, T. and G. K. Vallis. 2001. Linear stability analysis of three-dimensional thermally-driven ocean circulation: Application to interdecadal oscillations. J. Climate, *53A*, 526–545.

Levitus, S. 1989. Interpentadal variability of temperature and salinity at intermediate depths of the North Atlantic Ocean, 1970–1974 versus 1955–1959. J. Geophys. Res., *94*, 9679–9685.

Madec, G. and M. Imbard. 1996. A global ocean mesh to overcome the North Pole singularity. Clim. Dyn., *12*, 381–388.

Madec, G., P. Delecluse, M. Imbard, and C. Lévy. 1998. OPA 8.1 ocean general circulation model reference manual. Technical report, Institut Pierre-Simon Laplace (IPSL), France, No. 11, 91 pp.

Moore, A. M. and B. F. Farrell. 1993. Rapid perturbation growth on spatially and temporally varying oceanic flows determined using an adjoint method: Application to the Gulf Stream. J. Phys. Oceanogr., *23*, 1682–1702.

Moore, A. M. and R. Kleeman. 2001. The differences between the optimal perturbations of coupled model of ENSO. J. Climate, *23*, 138–163.

—— 1999. The non-normal nature of El Niño and intraseasonal variability. J. Climate, *12*, 2965–2982.

Moore, A. M., J. Vialard, A. T. Weaver, D. L. T. Anderson, R. Kleeman, and J. R. Johnson. 2003. The role of air-sea interaction in controlling the optimal perturbations of low-frequency tropical coupled ocean-atmosphere modes. J. Climate, *16*, 951–968.

Neelin, J. D., F. Jin, and H. Syu. 2000. Variations in ENSO phase locking. J. Climate, *13*, 2570–2590.

Rasmusson, E. M. and T. H. Carpenter. 1982. Variations in tropical sea surface temperature and surface wind fields associated with the Southern Oscillation/El Niño. Mon. Wea. Rev., *110*, 354–384.

Redi, M. H. 1982. Oceanic isopycnal mixing by coordinate rotation. J. Phys. Oceanogr., *12*, 1154–1158.

Sévellec, F., M. Ben Jelloul, and T. Huck. 2007. Optimal surface salinity perturbations influencing the thermohaline circulation. J. Phys. Oceanogr., *37*, 2789–2808.

Sévellec, F., T. Huck, M. Ben Jelloul, N. Grima, J. Vialard, and A. Weaver. 2008. Optimal surface salinity perturbations of the meridional overturning and heat transport in a global ocean general circulation model. J. Phys. Oceanogr., *38*, 2739–2754.

Sévellec, F., T. Huck, M. Ben Jelloul, and J. Vialard. 2009. Non-normal multidecadal response of the thermohaline circulation induced by optimal surface salinity perturbations. J. Phys. Oceanogr., *39*, 852–872.

Thompson, C. J. and D. S. Battisti. 2000. A linear stochastic dynamical model of ENSO. Part I: Model development. J. Climate, *13*, 2818–2832.

—— 2001. A linear stochastic dynamical model of ENSO. Part II: Analysis. J. Climate, *14*, 445–466.

Torrence, C. and P. Webster. 1998. The annual cycle of persistence in the El Niño-Southern oscillation. Q. J. R. Meteor. Soc., *124*, 1985–2004.

Tziperman, E., M. A. Cane, S. E. Zebiak, Y. Xue, and B. Blumenthal. 1998. Locking of El Niño's peak time to the end of the calendar year in the delayed oscillator picture of ENSO. J. Climate, *11*, 2191–2199.

Tziperman, E., S. E. Zebiak, and M. A. Cane. 1997. Mechanisms of seasonal - ENSO interaction. J. Atmos. Sci., *54*, 61–71.

Wallace, J. M., E. M. Rasmusson, T. P. Mitchell, V. E. Kousky, E. Sarachik, and H. von Storch. 1998. On the structure and evolution of ENSO-related climate variability in the tropical Pacific: Lessons from TOGA. J. Geophys. Res., *103*, 14241–14260.

Weaver, A. T., J. Vialard, and D. L. T. Anderson. 2003. Three- and four-dimensional variational assimilation with a general circulation model of the tropical Pacific Ocean. Part 1: Formulation, internal diagnostics and consistency checks. Mon. Wea. Rev., *131*, 1360–1378.

Xue, Y., M. A. Cane, S. E. Zebiak, and M. B. Blumenthal. 1994. On the prediction of ENSO: A study with a low-order markov model. J. Climate, *46A*, 512–528.

Zanna, L., P. Heimbach, A. M. Moore, and E. Tziperman. 2010. The role of ocean dynamics in the optimal growth of tropical SST anomalies. J. Phys. Oceanogr., *40*, 983–1003.

Zebiak, S. E. and M. A. Cane. 1987. A model of El Niño-Southern oscillation. Mon. Wea. Rev., *115*, 2262–2278.